A novel method and printhead for 3D printing combined nano-/microfiber solid structures

Kara Y., Kovács N. K., Nagy-György P., Boros R., Molnár K.

Accepted for publication in Additive Manufacturing
Published in 2022
DOI: https://doi.org/10.1016/j.addma.2022.103315

Additive Manufacturing 61 (2023) 103315

Contents lists available at ScienceDirect

Additive Manufacturing

journal homepage: www.elsevier.com/locate/addma

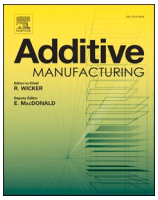

A novel method and printhead for 3D printing combined nano-/microfiber solid structures

Yahya Kara [a,*], Norbert Krisztián Kovács [a,b], Péter Nagy-György [c], Róbert Boros [a], Kolos Molnár [a,d,**]

[a] Budapest University of Technology and Economics, Faculty of Mechanical Engineering, Department of Polymer Engineering, Műegyetem rkp. 3., H-1111 Budapest, Hungary
[b] MTA-BME Lendület Lightweight Polymer Composites Research Group, Műegyetem rkp. 3., H-1111 Budapest, Hungary
[c] Budapest University of Technology and Economics, Faculty of Mechanical Engineering, Department of Hydrodynamic Systems, Műegyetem rkp. 3., H-1111 Budapest, Hungary
[d] ELKH–BME Research Group for Composite Science and Technology, Műegyetem rkp. 3., H-1111 Budapest, Hungary

ARTICLE INFO

Keywords:
Nanofiber
Nonwoven
Material extrusion
Airflow
Hierarchical structures

ABSTRACTS

In this study, we demonstrate a novel 3D printing method and printhead capable of 3D printing objects, which are combinations of nano-/microfibers and solid or infill layers. The method is a unique combination of material extrusion and melt-blowing: the filament can be fused and then either deposited or turned into ultrafine fiber mats with the aid of hot pressurized air. This study introduces the operation of the prototype device, the computational fluid dynamics (CFD) simulations of the airflow field, and various tests on the generated specimens. We were able to make layers of ultrafine fiber mats from poly lactic acid (PLA), which adhered to the solid deposited layers of the same PLA material. Higher air speed and smaller nozzle size resulted in smaller fibers. Fibers with a diameter of as small as 300 nm and an average of 900 ± 100 nm were generated at supersonic air velocities. The fiber layers enhance the crystallinity of the printed products, and can reinforce those. We can control the position and ratio of the fibers and the solid (or infill) parts of the printed object, so even porous objects can be generated. These hierarchical 3D printed objects have lots of possible applications, such as scaffolds, controlled drug delivery devices, filter media, structural composites and smart textiles.

1. Introduction

The interdisciplinary expansion of additive manufacturing (AM) has led to a growing demand for suitable materials and technologies [1]. Even though the COVID-19 pandemic caused a significant slowdown, the worldwide AM market for related products and services grew by 7.5% in 2020 [2]. Recent reports revealed that the AM industry was expanded by 19.5% in 2021 [3]. The distinct advantages, including but not limited to: reduction in manufacturing cost and process downtime, less waste, straightforward and single-step production, reliability and ease in developing customized engineering products, accelerated the extension of the AM industry and related end-products [4–6].

Fused filament fabrication (FFF) is one of the most popular AM methods due to its versatility, good value for money, and ease of maintenance [7]. In 2015, the FFF or material extrusion AM was defined by ISO/ASTM 52900 as "*An additive manufacturing process in which material is selectively dispensed through a nozzle or orifice*" [8]. The FFF consists of melting the thermoplastic feedstock in the print head (i.e., extruder assembly), and then the molten polymer is pressurized through the nozzle at a desired volumetric flow. FFF technology was invented in 1988 by Scott and Lisa Crump. In 1989, Crump patented [9] the first FFF method called fused deposition modeling (FDM). Crump then created the software process that converts Standard Tessellation Language (STL) files into another format to slice sections of the 3D model and determine how the layers will be printed. After Crump's invention, today's well-known companies like Stratasys, General Electric, HP, 3 M, 3D Systems, Markforged, Boeing, EOS, Xerox, and many others actively advanced and industrialized the FFF and related 3D printed parts for

* Corresponding author.
** Corresponding author at: Budapest University of Technology and Economics, Faculty of Mechanical Engineering, Department of Polymer Engineering, Műegyetem rkp. 3., H-1111 Budapest, Hungary.
E-mail addresses: karay@pt.bme.hu (Y. Kara), molnar@pt.bme.hu (K. Molnár).

https://doi.org/10.1016/j.addma.2022.103315
Received 22 October 2022; Received in revised form 11 November 2022; Accepted 22 November 2022
Available online 24 November 2022

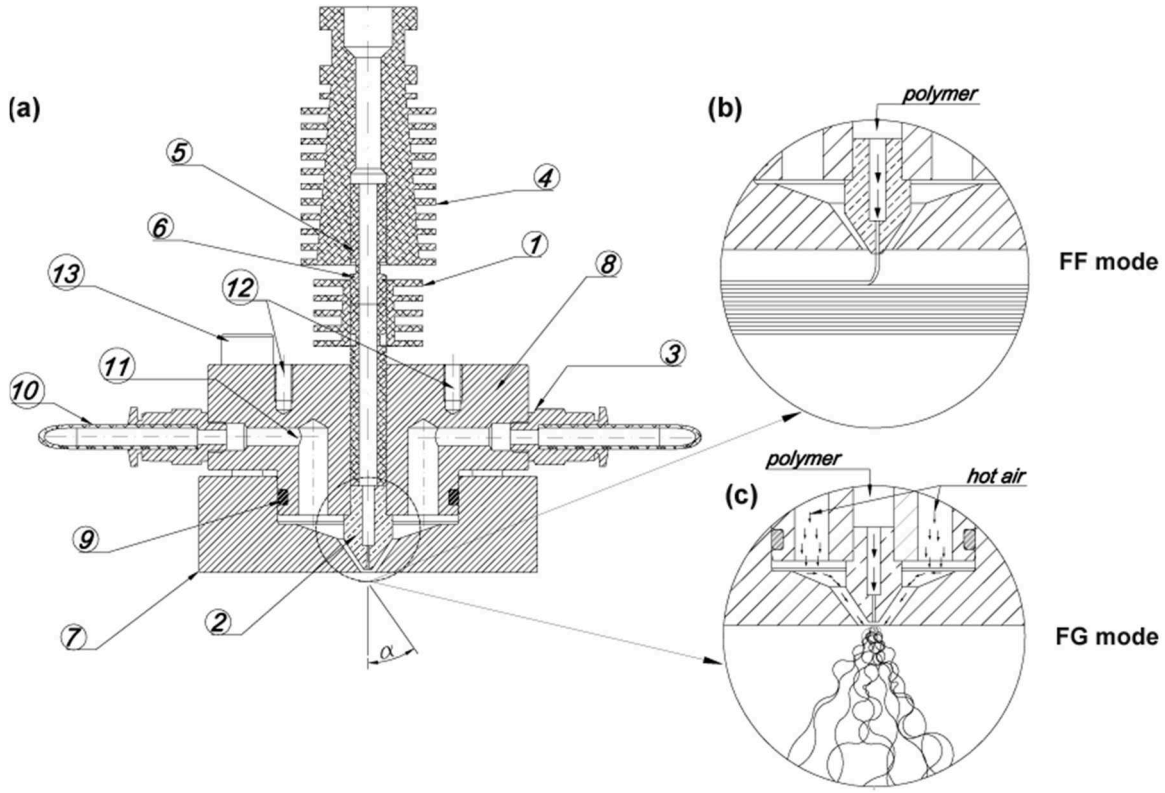

Fig. 1. Schematics of the developed FFF apparatus (a) A half-section view (1: heat sink, 2: nozzle, 3: air tube connector, 4: heat sink, 5: throat heat break, 6: throat heat break, 7: air knife module, 8: heated block, 9: O-ring, 10: air tube, 11: air channel, 12: assembly connectors. 13: bolt (leveling)), the demonstration of (b) filament fusion (FF) and (c) fiber generation (FG) mode operations.

years [2,10,11].

To date, many efforts have been paid to advance the manufacturing of complex structures via FFF 3D printing [12,13]. Nevertheless, pushing the limits toward generating ultrafine fibers and integrating them with printed structures via the FFF remains a great challenge. In the last two decades, many research activities have been done to develop strategies for FFF printing textile structures like nonwovens and nanofibers [14,15]. In this regard, novel methods like melt electrospinning writing (or melt electrowriting) (MEW) were developed using the fundamentals of AM combined with electrospinning [16,17]. It is rooted in traditional electrospinning, which is a technique that involves stretching a polymer solution or melt into nanofibers under a high electric field and accumulating it on the counter electrode in the form of a randomly oriented fiber web [18,19]. In MEW, the molten polymer is electrostatically drawn into the nano-/micro fibers towards a computer-controlled collector plate in a well-confined path with fairly good resolution. However, the need for sophisticated instrumentation and operation difficulties hamper MEW's applicability [20]. In addition, generating complex structures consisting of 3D print struts and fibers via MEW is not achieved so far. Farer et al. [21,22] took an innovative approach to fabricate seamless textiles by robotic fiber dispensing and assembly control. The method is rooted in melt blowing, for which the polymer melt is extruded through a die containing numerous small capillaries and then stretched via a jet of hot air [23]. The ratio of high-velocity air versus the lower velocity polymer provides a drag force that rapidly attenuates the forming fibers [24,25]. The robotic fiber assembly and control systems (RFACS) method aimed to deposit fiber mats onto a 3D collector to form a randomly aligned fine fiber web. Farer and coworkers [22] produced PP fibers with a traditional extruder and a robotic control system with an average diameter of around 10 μm. However, this method only allows generating fine fibers via robotic control, and it also requires expensive machinery and complex processing control to create 3D textile structures.

To date, several attempts have been made to commercialize 3D printing textiles. A UK-based company called TamiCare developed an AM-based process called CosyFlex [26]. Their technology involves customized 3D printing with textile fibers manufactured in layers by a spray jet. Another company from the USA, Electroloom, used AM and electrospinning methods to generate 3D-printed textiles [27]. Electroloom's approach used traditional electrospinning to generate fiber mats deposited onto a 3D mold (e.g., similar to RFACS). Although generating fibers via AM became real in the industry quickly, these companies fell short of commercialization expectations. This is because of the complexities and difficulties in implementing the proposed technology, being only available for fiber making, and high operational costs.

Creating complex structures via FFF consisting of nano-/microfibers and 3D printed struts has followed a separate multi-step process [28,29]. In these methods, a fibrous structure was produced, for example, via electrospinning and then incorporated into 3D print layers. Kozior et al. [30] studied a sequential spin-on method involving electrospinning in combination with FFF and material jetting (using photo-cured liquid polymer resins, a.k.a. PolyJet Matrix) to develop structures for medical applications. In their study, 3D-printed rectangular prisms are produced by FFF and material jetting, and then electrospun fibers are deposited onto them. Another method comprises alternating and repeating layer-by-layer material (e.g., hydrogel inks) dispensing combination with the insertion of prepared electrospun fiber mats between the layers during the printing process [31]. Yu et al. [32] proposed a novel approach composed of infusing electrospun nanofibers into 3D-printed meshes to make biocompatible composite scaffolds. Xu et al. [33] developed a unique bioprinting technique that uses tandem construction of material jetting (a.k.a. inkjet printing) and electrospinning head. Several research studies confirmed that incorporating fiber mat into a 3D-printed piece enhances the mechanical performance of the

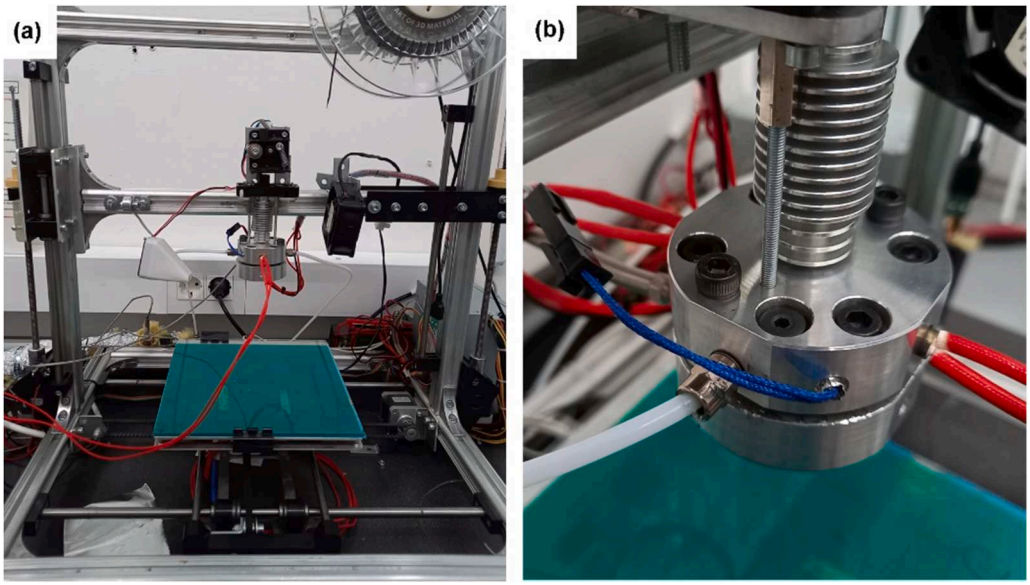

Fig. 2. Optical images of FFF printer assembly (a) Velleman 8200 FFF printer with the developed apparatus, (b) close look up to the developed apparatus.

3D-printed hierarchical composites [1,28,34]. However, the difficulties in the processing (e.g., incorporating a delicate fibrous layer), high cost, and low precision are some obstacles that hinder the applicability of creating hierarchical 3D printed composites via FFF. The current efforts are far from integrating these fibrous substrates' in a cost-efficient, high-speed and -throughput production system. The other issue is that generating such textile structures via AM is either expensive or requires advanced hardware, and besides, processing difficulties occur that hinder their wide use. Many approaches have been reported that are inaccessible to everyday users as these methods require either unique and expensive materials, machinery or customized hardware and software beyond conventional FFF printers [20,35]. Although some efforts have been devoted to FFF printing textiles structures (e.g., knitted meshes), the properties of those structures do not fulfill fundamental textile parameters, such as being light, porous, oriented, flexible, strong, permeable, etc. [36,37]. The ability to generate fine fiber structures and 3D printed struts with a single apparatus would possibly fit in numerous markets in automotive, aerospace, defense, medical, pharmaceutical, textile, etc. Yet, no process or tool was reported to generate fine fibers via the AM method and implement it into 3D printing with a single tool. Furthermore, creating complex FFF printed 3D structures with continuous nano-/submicron fibers directly from the feedstock (e.g., molten polymers) remains unfolded.

In this study, we introduced a novel FFF method that combines continuous ultrafine fibers and 3D print struts within a single object via a single apparatus. We demonstrated the applicability of the developed apparatus using a commercial desktop printer. We detailed the method and the respective FFF technology by testing the continuous fiber manufacturing and FFF printing struts. We first analyzed the fiber formation mechanism and detailed the airflow field using computational fluid dynamics (CFD) simulations. Then, we investigated the effect of the airflow field on the fiber-generating process, the resultant fiber morphology, and thermal and mechanical properties. We tested novel apparatus applicability for classical FFF 3D printing operation. Finally, hierarchical structures comprising fine fibers and 3D-printed struts were 3D printed and evaluated using SEM. Results revealed that the novel method of generating 3D print struts and nano-/micro continuous fibers with one single printing head could complement their respective advantages.

2. Materials and method

2.1. Method description

We invented a new approach and a FFF apparatus that generates nonwoven layers of nano-/micro fibers and fabricates hierarchical structures via FFF technology and patented it recently [38]. The printhead can generate both ultrafine fibers and struts. A half-section view of the apparatus is shown in Fig. 1(a). The opening between the heated block (8) and the air knife (7) can be adjusted by tightening and loosening bolts (Fig. S1). The opening between the heated block and the air knife allows the positioning of the nozzle inside or outside of the air knife module, as shown in Fig. 1(b-c) (Figs. S2 and 3). A heat-resistant *O*-ring (9) avoids air leakage during the operation. When the nozzle is inside the air knife and pressurized air is applied, the apparatus works in the continuous fine fiber generation (FG) mode, while filament fusion (FF) mode takes place when the nozzle is placed outside. In the prototype system, the screws are set manually; however, this motion can be automated. Based on the FFF printing nozzle (2) geometry and air exit annular orifice (Ø2.5 mm), the opening distance between the air knife module and the heated block was chosen as a minimum of 1 mm for smooth operation.

The developed apparatus does not require too expensive hardware; for example, the throat tube, brass nozzle and heat sink are commercially available for FFF printers. Just like in classical FFF printing, the filament is fed from a spool, passes through throat tubes (5,6), and reaches the moving heated block (8). The molten polymer is forced out of the nozzle (2). The molten polymer meets with hot air at the nozzle exit in the air knife module (7). The hot air fed through air tubes (10) passes vertical air slots (11) located in the heated block and reaches the nozzle tip (2) (Fig. 1(b-c)). With the developed apparatus, a commercial FFF printer with the necessary modifications can be used for both fiber making and filament fusion (Fig. 2, Figs. S3–6).

The novel apparatus consists of two major parts: the air knife module (7) and the heated block (8). The air knife module (7) has a conic geometry with a cone opening half-angle (α) that generates a high drawing force (Fig. 1). The air gap between the heated block and the nozzle represented by the α angle affects the air outlet velocity, the air temperature and the fiber attenuation rate. When the α angle is large, it results in fiber separation or high turbulence. On the other hand, a lower α angle yields roped fibers and loosely coiled bundles, which are undesirable [39,40]. Therefore, the cone opening half-angle of 35° and 60°

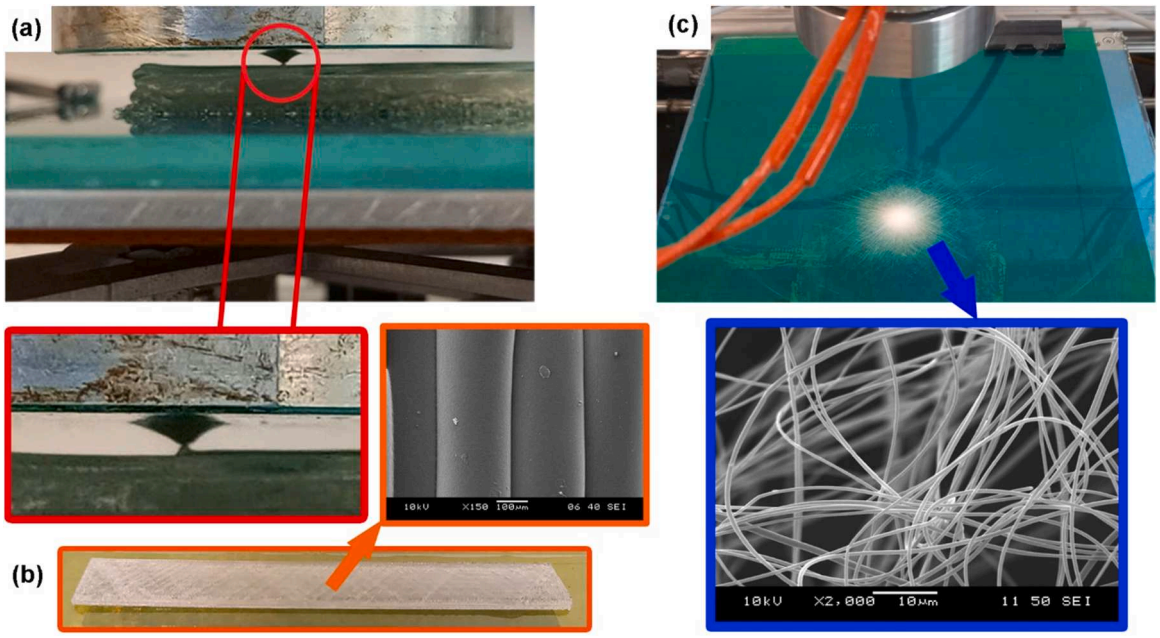

Fig. 3. Illustration of the operating modes; (a) Optical images of the FF mode (VIDEO 1), (b) printed object and SEM image of the struts and (c) optical image of FG process with the novel apparatus and SEM image of the generated nanofibers (VIDEO 2).

(i.e., air knife) was chosen to investigate for generating continuous fibers. The apparatus possesses a straightforward design that allows switching between FF and FG modes. The opening between the air knife module (7) and the heated block (8) can be adjusted by leveling bolts (Fig. S1). Therefore, hierarchical structures can be generated by FF and FG modes of operation continuously. The developed method and apparatus facilitate generating 3D printed parts and fine fibers via FFF technology, as shown in Fig. 3.

Supplementary material related to this article can be found online at doi:10.1016/j.addma.2022.103315.

Unlike traditional extrusion-based fiber-making methods such as melt-blowing technology, the developed apparatus generates fibers from thermoplastic filament extruded through a heated short length (*e.g.*, 35 mm) without using an extrusion screw (Fig. 3). The apparatus uses a FFF filament as the raw material as it is used in FFF 3D printing. The apparatus can generate fibers without an extruder screw (i.e., traditional extrusion-based fiber spinning methods require an extruder with a screw), and this extinct difference makes the method novel, while it allows FFF print structures (FF mode) from the same material used for FG mode. This feature also allows FFF printing of structures and fine fibers without employing expensive hardware or software (Figs. S3 and 4). Introducing a functional nano-/submicron fiber mat via FFF printing of the filament layers can bring potential benefits, such as a more flexible and cost-effective production of advanced engineering structures via FFF. For example, a potential application can be tissue engineering, where the scaffold's desired mechanical performance and custom geometry can be ensured by the solid parts of the body, while the cells can adhere better to the fiber structure [41,42].

2.2. Ansys airflow field simulations

Several attempts have been devoted to analyzing the free jet using various methods such as CFD [43], numerical stability analysis [44,45] and experimental measurements [46]. In this study, we chose the CFD technique, which is validated by experimental measurements due to its general applicability and high accuracy [47–50]. We investigated the airflow field formed in FG mode by CFD simulations performed with Ansys CFX 2019R3 software. The same material properties, boundary conditions and numerical settings were used as they were in the real-time experiments.

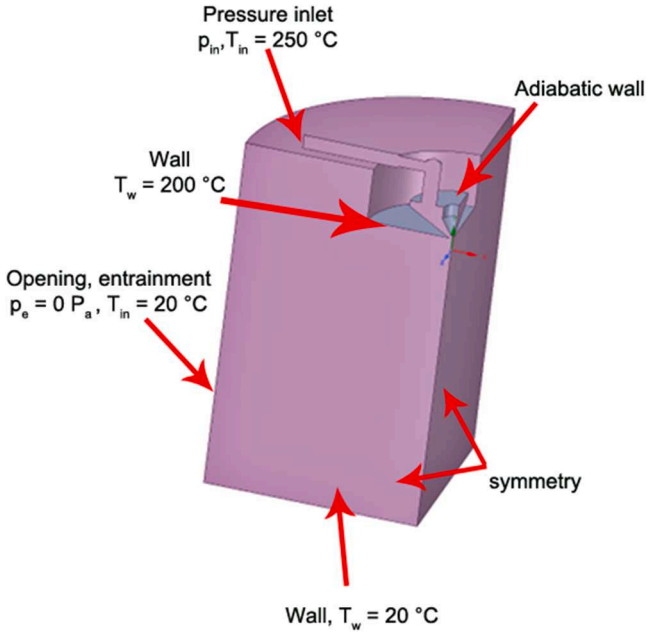

Fig. 4. The quarter model of the flow field and the environment with the corresponding boundary conditions.

2.2.1. Meshing

Fig. 4 depicts the CFD model's geometry data and boundary conditions. One-quarter of the whole geometry was modeled using symmetry simplification to reduce the computational cost. The structured mesh had hexahedra elements in the inflation layer near the wall and tetrahedra cells inside the flow domain (Fig. S7). The inflation layer was 0.2 mm in width and contained 5 layers with a growth rate of 1.2. The mesh is refined inside the apparatus and in the vicinity of the apparatus orifice.

To eliminate the discretization error, mesh independence analysis

Table 1
The summary of the boundary conditions.

Boundary condition	Validation of pressure loss	Validation of temperature field	Experimental setup parameters
Inlet	$T_{in} = 20$ °C $p_{in} = 0.4$–2.4 bar	$T_{in} = 250$ °C $p_{in} = 1;1.5$	$T_{in} = 250$ °C $p_{in} = 1;1.5;2$ bar
Apparatus inside walls	Adiabatic No-slip		
Apparatus outside walls	$T_{wall} = 20$ °C No-slip	$T_{wall} = 200$ °C No-slip	$T_{wall} = 200$ °C No-slip
Fiber collector plane	$T_{plane} = 20$ °C No-slip		
Environment	$T_{env} = 20$ °C $p_{env} = 0$ bar		

was performed with three different mesh sizes. We tested 1456k, 2998k, and 6782k elements for the air knife with a half-cone opening angle of 60°, and we compared the obtained air flow rate values to the measurement data. The results show that the relative difference in the obtained values was less than 1% in the case of these three meshes. Considering simulation time and the small difference between the simulation and experimental results, the mesh with 2998k cells was chosen for further simulations.

2.2.2. Boundary conditions

The heated and pressurized air flows into the apparatus at the inlet described with a p_{in} relative pressure and T_{in} temperature. It is assumed that there is only a short time for heat exchange due to the high velocities; therefore, the heat transfer inside the nozzle was neglected. The apparatus inside walls were modeled with adiabatic no-slip walls. Based on the empirical observations, the outer wall temperature was assumed to be $T_{wall} = 200$ °C and $T_{wall} = 20$ °C for the heated and non-heated cases, respectively. The environment was represented by the opening boundary condition with $T_{env} = 20$ °C temperature and $p_{env} = 0$ Pa entrainment pressure. The fiber collector plane was considered with a 20 °C, no-slip wall.

For validation purposes, two independent cases were considered. In the first case, the volume flow rate was calculated when the inlet temperature was equal to ambient, $T_{in} = T_{env} = 20$ °C, and the pressure varied between 0.4 and 2.4 bars. In that case, the outer wall of the apparatus was $T_{wall} = 20$ °C. In the second case, the temperature distribution was determined when $T_{in} = 250$ °C and p_{in}= 1 and 1.5 bar. For that, the outer apparatus wall temperature was $T_{wall} = 200$ °C. Finally, these two cases were combined to validate experimental observations, for which $p_{in} = 1;1.5;2$ bar, $T_{in} = 250$ °C, and $T_{wall} = 200$ °C values were applied.

Table 1 summarizes the applied boundary conditions.

2.2.3. Material properties and turbulence model

The air was considered to be an ideal gas with $\mu = 1.831 \cdot 10^{-5}$ Pa·s dynamic viscosity, $\lambda = 0.0261$ W/(mK) thermal conductivity and $c_p = 1004.4$ J/(kgK) specific heat (at constant pressure) at 25 °C reference temperature. Because the computational domain contains narrow (inside the apparatus) and large far-field (outside the apparatus) regions, the Shear Stress Transport (SST) turbulence model was applied with an automatic wall function. As a result, a set of equations for the continuity, energy, momentum, turbulent eddy frequency and turbulence kinetic energy were solved.

Since the real application is time-independent, steady-state simulations were performed with high-resolution advection and first-order turbulence schemes. The convergence criteria were set to 10^{-5}, while the volume flow rate was monitored. The simulation stopped when the convergence criteria and the steady-state solution of the volume flow rate were reached.

2.2.4. Air temperature and flow rate measurement

To verify the airflow field CFD model, we measured and predicted the effects of air knife design and air pressure on velocity and temperature distributions. We conducted experiments to measure the airflow rate at the apparatus inlet and the air temperature after air exits the heated block. We measured the temperature in-line, with a K-type bare thermocouple and a digital thermometer (Testo 830-T2, Germany). The thermocouple was placed parallel to the apparatus to read the air centerline temperature. With this aim, the thermocouple was set and fixed to variable distances (5–40 mm) from the apparatus during the experiments. The temperature was recorded when the read value reached a stable region, e.g., ± 1 °C. A thermal camera (A325sc, FLIR Systems Inc., Wilsonville, OR, USA) was also used to monitor apparatus temperature during the operation. A digital flowmeter (flow switch, PFMB721-C8-F, SMC, Japan) was used to measure the air volume flow rate. The measurement setup used is shown in Fig. S8.

We measured the volume flow rate and the temperature field separately, because the flowmeter used was unsuitable for operating at high temperatures. Firstly the air volume flow rate without heating was measured at room temperature. The inlet air pressure was set in the 0.4–2.4 bar range using a pressure regulator (MS2-LFR, Festo, Germany), and the corresponding flow rates were recorded. According to the datasheet of the flowmeter, the recorded volume flow rate values correspond to the standard condition (T = 15 °C, p = 101.3 kPa), where the density is $\rho_{airstd} = 1.225$ kg/m^3. The recorded air volume rate value was converted to the mass flow rate $\dot{m}_{meas}$ using Eq. (1).

$$\dot{m}_{meas} = q_{airstd}\rho_{airstd} \tag{1}$$

where q_{airstd} is the measured volume flow rate corresponding to the standard conditions. The relative error between the CFD simulations and the measured flow rate was calculated using Eq. (2).

$$\varepsilon = \frac{|\dot{m}_{meas} - \dot{m}_{CFD}|}{\dot{m}_{meas}} \tag{2}$$

where $\dot{m}_{CFD}$ is the mass flow rate calculated via CFD computations.

2.3. Materials

A PLLA homopolymer (Total Carbion, Luminy® L105, MFI: 70 g/10 min at 190 °C, 2.16 kg) granules were used to prepare filaments for FFF 3D printing. The PLLA granules was dried in a WGL 45B oven (Huanghua Faithful Instrument, China) at 100 °C for 4 h before processing.

2.4. FFF filament production

We made filaments from PLLA granules mentioned above to generate fibers and 3D print structures with the same device. PLLA filaments (filament diameter 1.75 mm) were produced with a Precision 450 type filament maker (3devo B.V., The Netherlands). The desktop extruder consists of 4 heating zones. The filament was extruded through the nozzle and then cooled by multiple ventilators after the nozzle. The filament diameter was computer controlled by DevoVision App provided by the desktop extruder producer. The filament diameter was measured by an optical sensor before it was wound up onto the spool. The temperature profile was set to 185–210–195–185 °C (from hopper to die). The extruder screw rotation speed was set to 2.4 rpm.

2.5. Fused filament fabrication (FFF) device and experimental setup

A Velleman K8200 desktop FFF printer (Velleman vn., Belgium) was used to test the developed apparatus (Fig. 2 and Fig. S3). Two K-type thermocouples, one mounted to the air knife module (7) and the other mounted to the heated block (8), and a PID control unit was used to heat up and control the apparatus temperature, respectively. We used the

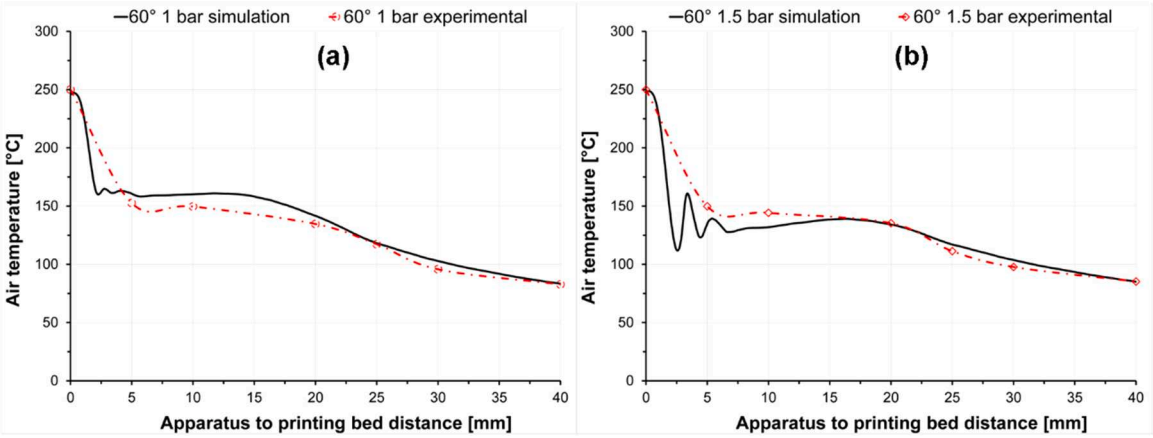

Fig. 5. Comparison of the CFD and experimental air temperature data at the applied air pressure of (a) 1 bar and (b) 1.5 bar.

open-source Printrun 2. X software (Pronterface, GNU General Public License) for controlling the FFF printer via computer.

In the FG mode, the apparatus temperature was set to a constant 200 °C. The desired air temperature (250 °C) was provided by an inline heater (AHPF-082, Omega, UK) and a K-type inline nozzle thermocouple and a PID controlling unit. The distance between the apparatus and the printing bed was set constant at 100 mm for fiber generating, while for FF mode it was 50 μm. The filament feeding speed was set to 1 mm/min. The nozzle diameter of 0.2, 0.4 and 0.5 mm were tested. The influence of three air pressure levels (1, 1.5 and 2 bar) and two air knife angles (35°and 60 °) on the fiber properties were tested.

2.6. Tensile tests

We prepared rectangular fiber mat samples in 40 mm × 10 mm size. The fiber mat length and width were measured using a micrometer (Louis Schopper Leipzig, Germany) with 0.01 mm precision. We weighed and recorded the PLA fiber mats using a Sartorius Quintix 1^{25}D–^{1}CEU (Sartorius, Germany) semi-micro scale. We calculated the fiber mat area by using Eq. (3).

$$A = \frac{m_{fm}}{l_{fm}\rho_{Polymer}} \tag{3}$$

where, m_{fm} is the fiber mat mass, $l_{fm}$is the length of the fiber mat and $\rho_{Polymer}$ is the polymer bulk density (e.g., PLA=1.24 g/cm^3).

The tensile properties of the fiber mats were tested at room temperature with a Zwick Z005 (Zwick, Germany) type universal tensile tester equipped with a 20 N load cell. The gauge length and tensile speed were 20 mm and 10 mm/min, respectively. The testing routine was performed 6 times for each sample group.

2.7. Differential scanning calorimetry (DSC) tests

The thermal properties of the fiber mats and the filament were studied by differential scanning calorimetry (DSC) with a Q2000 DSC (TA Instruments, USA) device. The heat-cool-heat tests were performed in an inert atmosphere (N_2; 50 ml/min purge flow rate) in a temperature range of 0–250 °C with a heating and cooling rate of 5 °C/min. The degree of crystallinity (χ) of the samples was determined based on Eq. (4). Based on ref. [51] 97 J/g was taken as the heat of fusion of the 100% crystalline (ΔH_m^0) PLA in the analysis (Eq. (4)):

$$\chi = \frac{\Delta H_m - \Delta H_{cc}}{\Delta H_m^0} \times 100[\%] \tag{4}$$

where, ΔH_m is the experimental heat of fusion and ΔH_{cc} is the experimental cold crystallization obtained by the DSC scans. We analyzed the glass transition temperature (midpoint temperature) samples of samples according to ASTM E1356–08 [52].

2.8. Producing 3D printed samples with the novel apparatus

We tested the developed apparatus's capability to create hierarchical structures, for which we produced FFF printed samples using FF and FG modes. The accuracy between the CAD model and printed parts was also investigated [53,54]. We used SolidWorks 16 (Dassault Systèmes, France) to design the 3D model sample with dimensions of 80 × 10×1.5 [mm] (length x width x thickness). The 3D model was converted to the ". STL" file format using SolidWorks 16. Then, CraftWare 1.21 slicing software (Craftbot, Hungary) was used to construct the model based on the settings of the 3D printer (Fig. S9). The same printer and software described in Chapter 2.5 were used to 3D print samples. The apparatus and printing bed temperatures were set to 200 °C and 60 °C, respectively. The nozzle diameter and filament drawing speed were 0.2 mm and 60 mm/s, respectively. Infill density was set at 25%. The 3D printed samples were compared in terms of geometry and precision with the 3D CAD model. We produced 5 samples and measured the 3D-printed sample's length, thickness and width with a precision of 0.01 mm using a digital caliper (Fowler Promax, USA).

2.9. Scanning electron microscopy (SEM)

The samples' morphology was observed using scanning electron microscopy (SEM; JEOL 6380 LA, Japan). Samples were pasted onto metallic studs with double-sided conductive tape. The sample surface was finely coated using a JEOL JFC-1200 (Jeol Ltd., Japan) fine coater with gold (Au) in order to avoid their charging. We measured 100 fibers for each sample to analyze the fiber diameter distributions. We used ImageJ 1.51k software for this measurement.

3. Results and discussion

3.1. Analyzing the airflow characteristics

3.1.1. Validation of the CFD model

Since the developed method possesses aerodynamically-driven fiber stretching, the motion of the polymeric jet and the fiber characteristics are assumed to be rooted in the aerodynamics of the airflow field (temperature, velocity, turbulence intensity, etc.) [47,55]. Therefore, computational fluid dynamics (CFD) simulations were employed in the FG mode to model the airflow field at the air outlet. We also conducted experimental air temperature and airflow rate measurements to correlate those with CFD simulation results. The CFD and experimental air temperature data are shown in Fig. 5. We measured 7 points at 5–40 mm

Table 2
Air mass flow rate data obtained from experiments and CFD simulations.

Air pressure [bar]	Experimental air flow rate [L/min]	$\dot{m}_{calculated}$ [g/s]	$\dot{m}_{CFD}$ [g/s]	Relative error [%]
0.39	59	0.91	1.07	14.7
0.67	82	1.26	1.37	7.9
1	105	1.60	1.73	6.9
1.35	128	1.96	2.11	7.2
1.68	150	2.27	2.47	8.1
2.02	172	2.58	2.84	9.2
2.38	196	2.92	3.24	9.8

distance from the tool tip with the thermocouple. We also monitored the apparatus temperature while the hot pressurized air (250 °C) was flowing. In addition, the apparatus temperature was continuously monitored via the printer interface (with an additional K-type thermocouple attached to the apparatus) and with a thermal camera (Fig. S10). The results implied that the difference between the CFD and experimental data was reasonable; hence, we concluded that CFD results could be used to model the airflow field and related process parameters.

We also measured the airflow rate (in L/min) with a flow meter when no air heating was applied. We analyzed the air's mass flow rate obtained by experimental and CFD analysis. The results are given in Table 2. Our findings showed that the relative error between the CFD and mass flow rate data determined by experimental ways was fairly small (<10%). We investigated the pressure loss characteristics between the CFD and the experimental data. The results showed that the CFD mass flow rate regime also correlates with the experimental data and expresses fair agreement (Table 2 and Fig. S11). In conclusion, CFD simulations can be used to estimate airflow characteristics with reasonable accuracy.

3.1.2. Results of the application-oriented CFD model

We investigated the effect of air pressure (1, 1.5 and 2 bars) and the cone opening angle (35° and 60° was chosen) on the air temperature (Figs. 6 and 7) and the air velocity field. The results implied that the air temperature drops faster near the apparatus when the air pressure increases; hence, the temperature gradient close to the die affects the final fiber properties (*e.g.*, fiber-to-fiber contacts, fiber mat thermal and mechanical properties, fiber crystallization and attenuation rate) dramatically. For example, when the air cools down fast, it provides a quicker

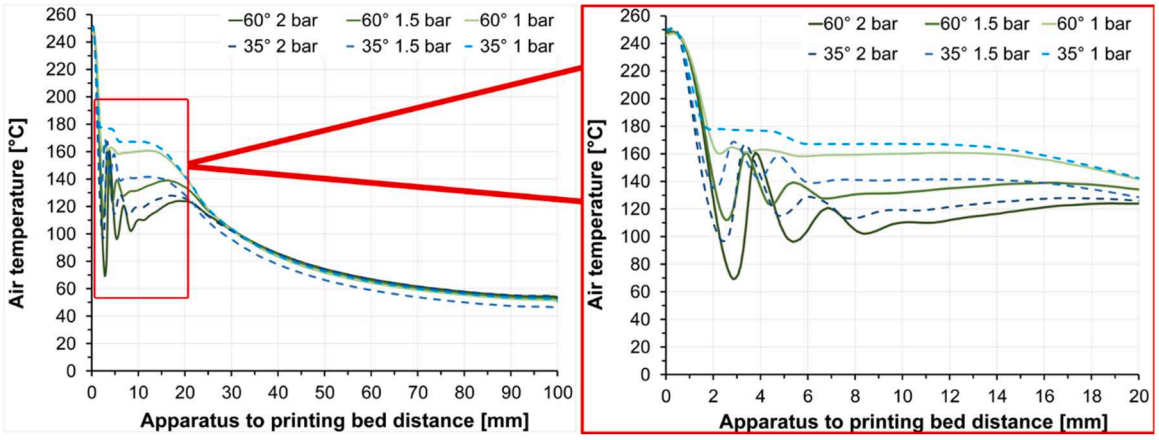

Fig. 6. Variation of the air temperature upon exiting the die for the air knife with half-cone opening angles of 35° (blue-colored dashed lines) and 60° (green-colored continuous lines) at various pressure levels.

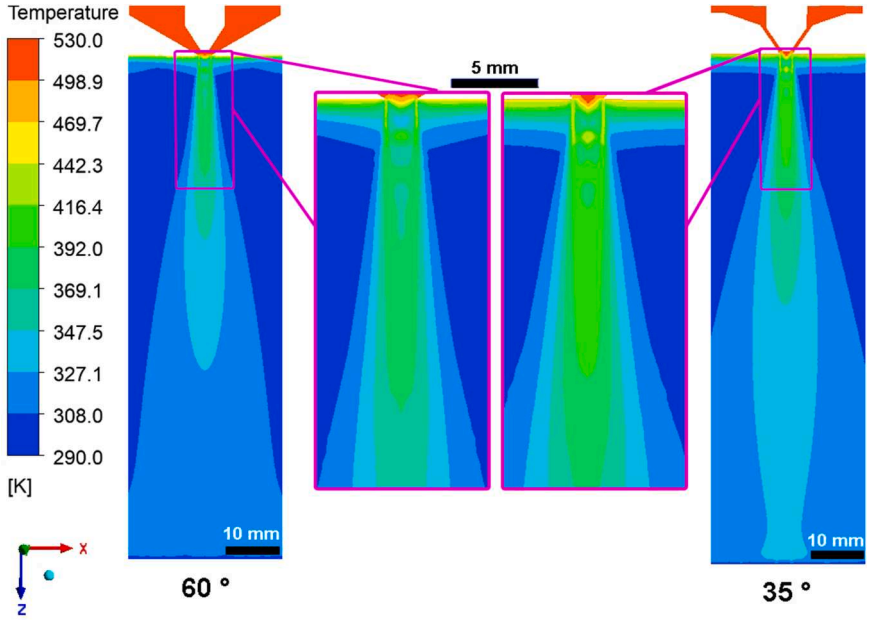

Fig. 7. Counter plots of air temperature profiles for the air knife with half-cone opening angles of 60°and 35° at the air pressure of 2 bar.

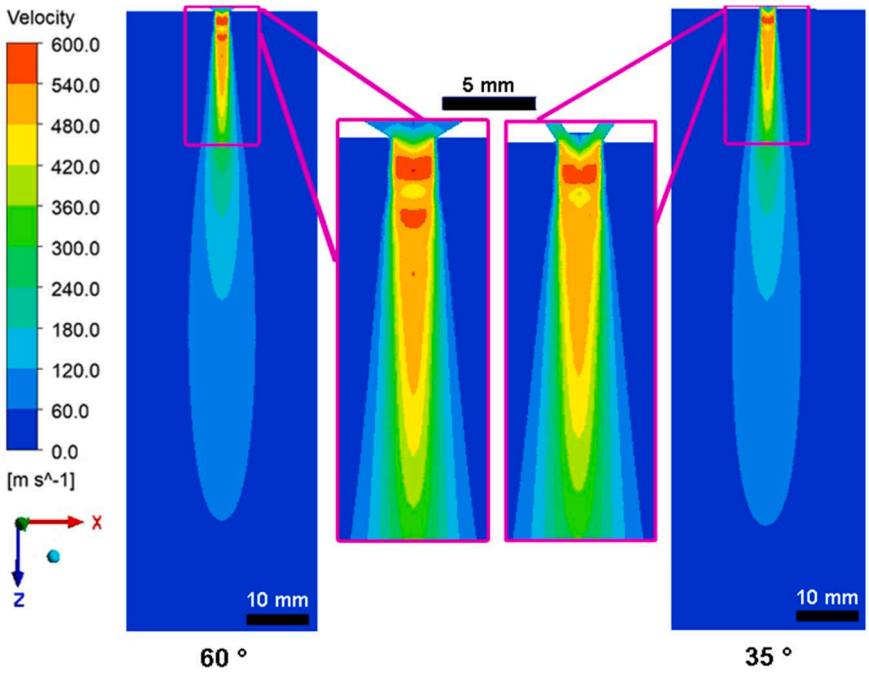

Fig. 8. Counter plots of air velocity profiles for the air knife with half-cone opening angles of 60° and 35° at the air pressure of 2 bar.

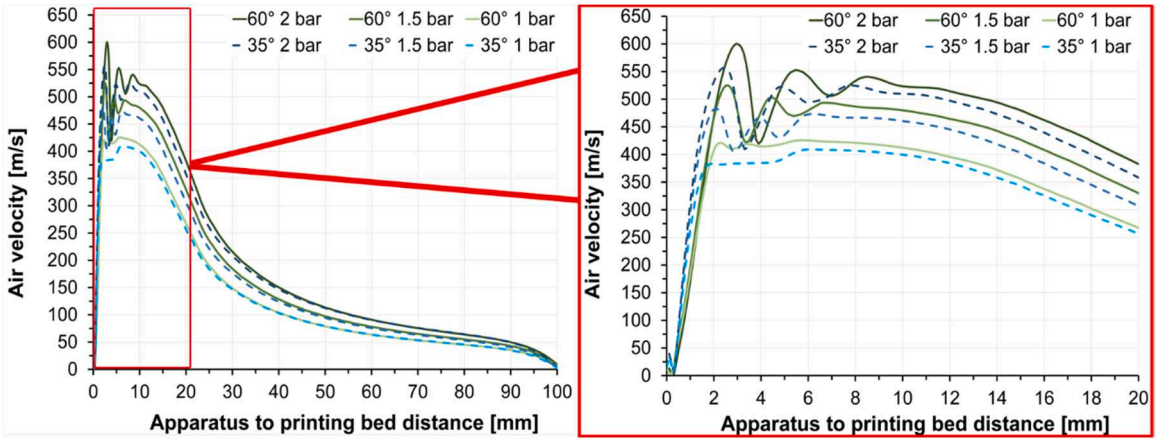

Fig. 9. Variation of the air velocity upon exiting the die for the air knife with half-cone opening angles of 35° (blue-colored dashed lines) and 60° (green-colored continuous lines) at various pressure levels.

solidification of the fibers, giving poor fiber bonding. However, air velocity also plays a vital role in the fiber structure development via the drawing it provides [24].

The results showed that the air cools down slower after exiting from the 35° air knife. This is related to the air velocity, which is slower in the case of the 35° half-cone opening angle. The 60° air knife exhibited lower air temperatures and higher air velocities than the 35° one for each pressure level. In this regard, we observed a region where the air

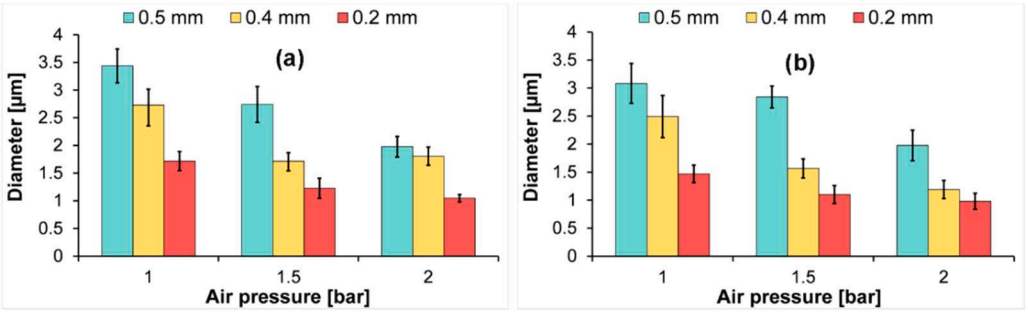

Fig. 10. Variation of fiber diameter versus air pressure and nozzle diameter; (a) fibers produced with air knife module with cone opening angle of 60° and (b) 35°.

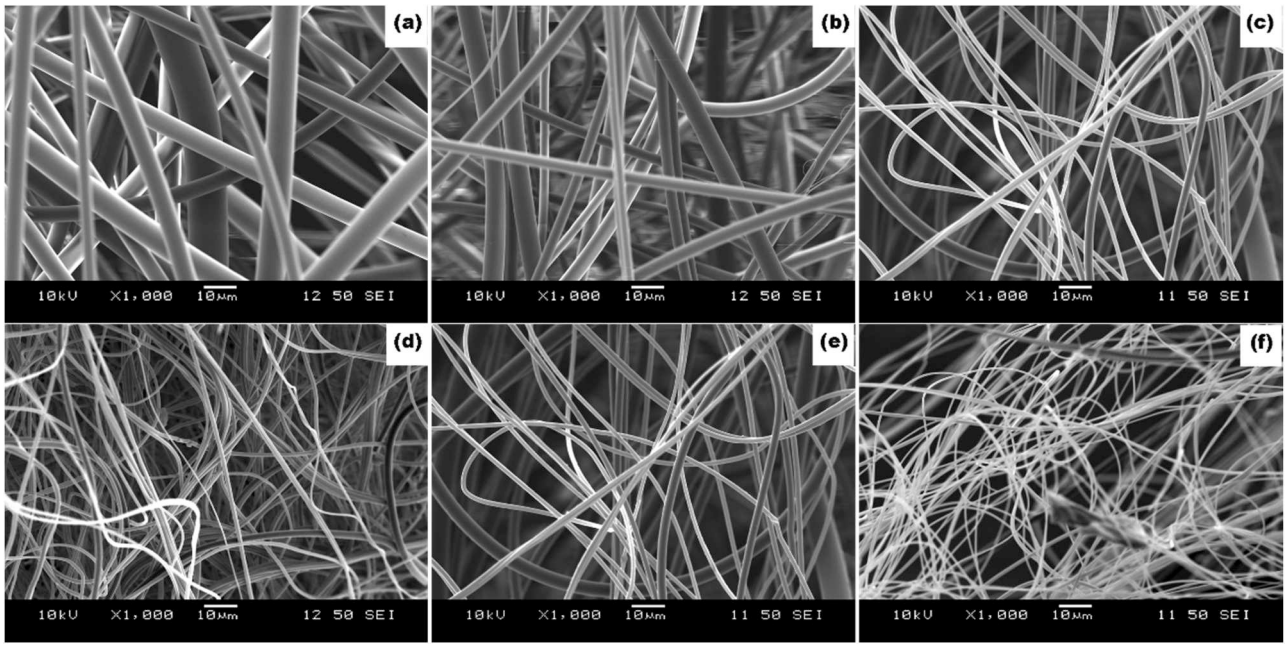

Fig. 11. SEM images of fibers. Effect of nozzle diameters of (a) 0.5 mm, (b) 0.4 mm, (c) 0.2 mm at 1.5 bar air pressure, and effect of air pressure (a nozzle diameter of 0.2 mm) of (d) 1 bar, (e) 1.5 bar, (f) 2 bar on fiber mat morphology produced.

jets converge for higher pressures, as shown in Figs. 6–9. This phenomenon results in air velocity and temperature fluctuation near this location. When the air velocity reached over 450 m/s for high inlet pressures (e.g., at 2 bar), the air jets near the apparatus converged and a velocity and temperature fluctuation appeared. The CFD simulations implied that air velocity for the 60° tool could reach as high as 1.62 Mach (~600 m/s), while the 35° tool had a max of 1.41 Mach (~550 m/s) when applied air pressure was 2 bar (Figs. 8 and 9, Fig. S12).

This fluctuation is associated with high turbulence kinetic energy [48,56]. Increasing the inlet air pressure resulted in high turbulence intensity, so the air velocity and temperature fluctuated over the distance (Fig. S13). For the 60° angle, we observed two maxima (i.e., negative and positive) in the region where the air jets converged for the air velocity field (Figs. 8 and 9). This might increase the fiber attenuation rate. On the other hand, the results implied that the 60° air knife possesses faster air cooling due to its high-velocity airflow.

3.2. Fiber mat morphology

We generated fine fibers with the apparatus in the FG mode and investigated the influence of nozzle diameter and air pressure on the fiber morphology. Fig. 10 shows the variation of the fiber diameter with respect to the nozzle diameter and the air pressure, while the fiber diameter distribution histograms are given in Figs. S14 and S15.

We found that a smaller nozzle diameter resulted in thinner fibers with fewer defects, as also shown in Fig. 11(a-c). Decreasing the nozzle diameter from 0.5 mm to 0.2 mm decreased the fiber diameter by up to 2.6-fold and 2.25-fold for the 60° and the 35° air knives, respectively. This is because the same drag force provided by the pressurized hot air jet was applied to a higher polymer mass. Besides, higher shear rates are favorable for attenuating the polymeric jet into fine fibers. The smaller capillary diameter generates higher shear rates on the melt. In the case of thermoplastic polymers, high shear rates are desirable for the polymer melt to be drawn into fine fibers because these are typically shear-thinning materials. The fiber attenuation rate was higher in the 60° air knife case than in the 35°. This is because the air velocity, so the drawing force, was higher in the 60° air knife case (see Fig. 9).

Results showed that a smaller nozzle diameter and high air pressure are favorable for generating continuous, evenly distributed, defect-free, thin fibers with the novel apparatus (Fig. 11(d-f)). Higher air velocity translates to larger attenuation rates. The air exerts a higher forwarding drag force and stress that draws the polymeric jet into a fine fiber. The average fiber diameter produced with the 60° air knife was 7–12% thinner than that produced by the 35° one. We found that increasing air

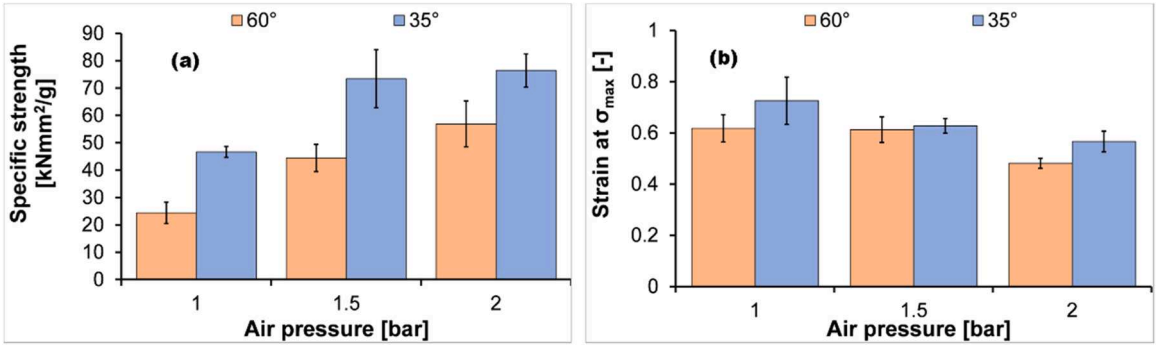

Fig. 12. Tensile properties of the fiber mats produced by cone opening angles of 60° and 35° (a) specific strength versus applied air pressure and (b) stain at σ_{max} versus applied air pressure.

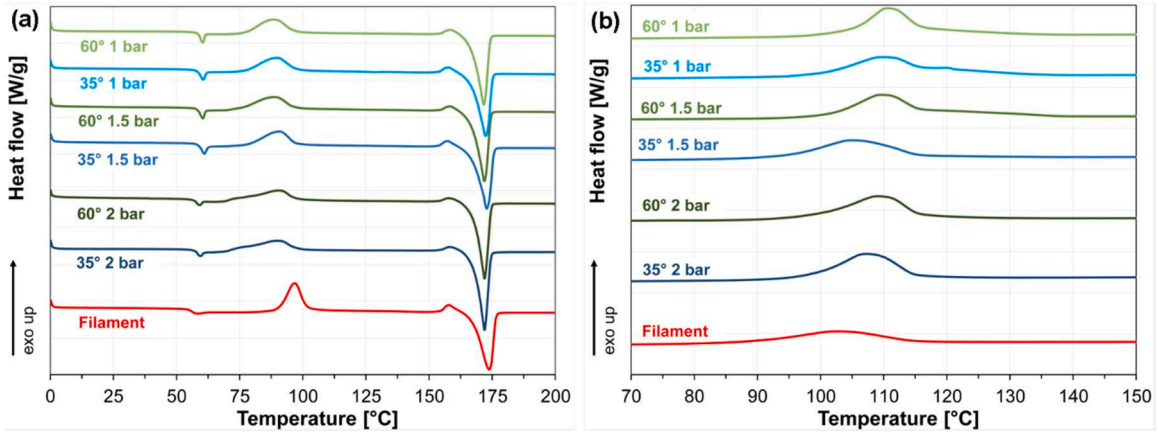

Fig. 13. Fiber mat's DSC thermograms; (a) 1st heating and (b) cooling cycles.

Table 3
DSC 1st heating data of the fiber mats and filament.

α [°]	Applied air pressure [bar]	Glass transition temperature, T_g [°C]	Cold crystallization enthalpy, $\Delta H_{cc1} + \Delta H_{cc2}$ [J/g]	Crystalline melting enthaply ΔH_m [J/g]	Degree of crystallinity, χ [%]
60	2	58.0	25.5	58.1	33.7
	1.5	58.8	28.7	58.7	31.0
	1	58.4	29.7	56.6	27.7
35	2	58.3	26.9	55.8	29.8
	1.5	58.6	31.9	60.2	29.1
	1	58.3	28.8	59.0	31.1
filament (reference)		54.6	32.2	59.3	28.0

pressure from 1 to 2 bar decreased the average fiber diameter by 50–110% for the 60° air knife. On the other hand, the average fiber diameter decreased by 51–75%, increasing air pressure from 1 to 2 bar for the 35° air knife.

These results are in-line with the CFD simulation findings. The air velocity and the temperature fields for the different cone opening angles and inlet air pressures resulted in different fiber and fiber mat properties. These findings prove that the novel apparatus provides straightforward manipulation of the fiber characteristics in a wide range.

3.3. Evaluating fiber mat's thermal and mechanical properties

The fiber mats produced via the novel apparatus with a nozzle diameter of 0.2 mm showed thin fibers with fine morphology. Therefore, we chose the nozzle diameter of 0.2 mm to investigate the fiber mat's thermal and mechanical properties. Results showed that increasing pressure increased the fiber mat's specific strength. This is because of increasing fiber packing density and thinner fibers generated with increasing air pressure, as shown in Fig. 12 (Fig. S16 and Table S1). A mechanically consolidated fiber mat structure accompanies the improved specific strength. On the other hand, increasing air pressure resulted in more fiber entanglements and lowered the fiber mat's strain at break and maximum stress.

The specific strength of fiber mats produced with a cone opening angle of 60° was lower than that of produced with the 35°. This difference is related to the cooling of the fiber. Fine fibers' microstructure development and crystallinity are mainly related to jet cooling and attenuation rate. Therefore, we conducted DSC tests for fiber mats and filaments to analyze their thermal properties. DSC thermograms are shown in Fig. 13. The 1st heating data obtained are given in Table 3, while the cooling and 2nd heating data are given in Table S2. DSC findings showed that the fibers' glass transition temperature and crystallinity are 4 °C and 6% points higher, respectively than those of the filament. These improvements are attributed to the shear-induced crystallization and increased molecular orientation along the thread line [25,57,58]. That is an advantage in keeping the structural integrity of the fibers when the 3D printer adds the next layer of dispensed molten material during the process.

Results showed that the fibers generated by the 60° air knife showed a higher degree of crystallinity for the same air pressure applied than the 35° one, which is related to the higher attenuation rates (i.e., air velocity). Findings implied that the fibers generated at high air pressure also showed a higher degree of crystallinity. In general, a higher degree of crystallinity translates to better mechanical properties. This is not the case in the case of fiber mats produced via the novel method. The DSC data represents microstructural development (e.g., molecular orientation, crystallinity) in fiber making. On the other hand, the conducted tensile tests represent the macroscale properties of the fiber mat. DSC cooling results revealed that the PLLA fibers showed different crystallization kinetics due to the high shearing applied. This is attributed to shear-induced nuclei formed during the FG mode. A similar finding has also been reported by Du et al. [57] in which they observed improved crystallization peak temperature for high-shearing applied PLLA in the DSC cooling curve. They concluded that a shish-like oriented structure due to high-shearing melt allows crystal growth at higher temperatures. These findings suggest that the PLLA fibers generated at different air pressures and half-cone opening angles had different nucleation kinetics subjected to different shear and melting conditions, resulting in different crystallization peak temperatures during DSC cooling cycles.

Overall, the DSC findings implied that the fibers had a different microstructure development compared to the filament. This also indicates that the FG mode is suitable for making fine polymeric with enhanced thermal stability.

The simulation study showed that the 60° cone opening angle possesses a higher air velocity (i.e., high attenuation rate) than the 35° one and cools down the air faster. A high attenuation rate improves the crystallinity, but high air velocity causes a faster cooling of both the air and the forming fiber. This, in turn, gives poor fiber-to-fiber contacts. The newly formed fiber's ability to penetrate those fibers collected at the printing bed affects the fiber mat's load-bearing capability. Higher attenuation rates (*e.g.*, higher air pressures) could compensate for the loss in mechanical properties with improved crystallinity and thinner fibers with an increased number of fiber entanglements.

3.4. Analyzing the novel apparatus FFF printing ability: Tests on the generic 3D samples

The developed apparatus can be used to generate continuous fibers

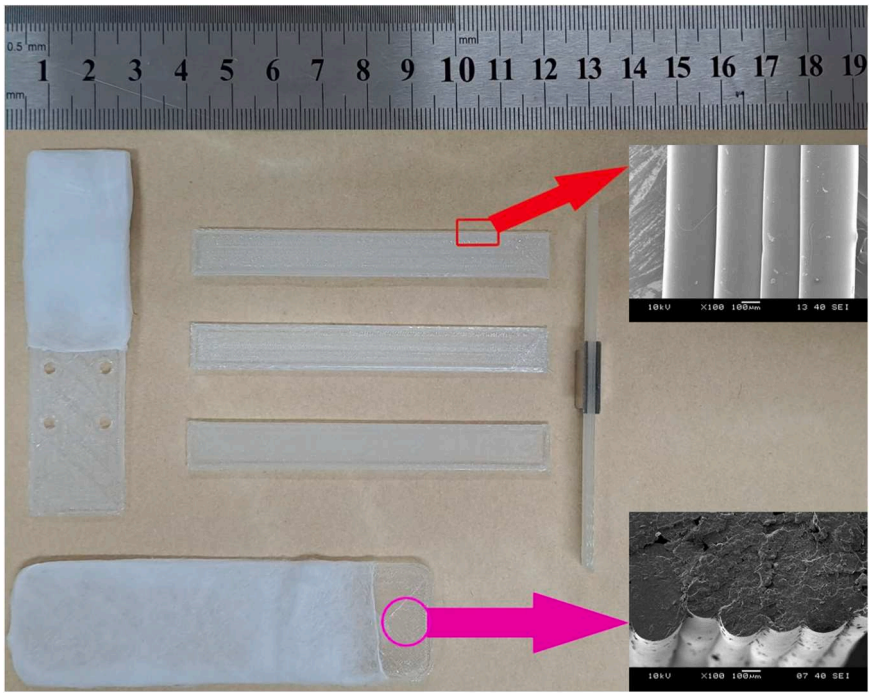

Fig. 14. Generic objects printed via novel printhead.

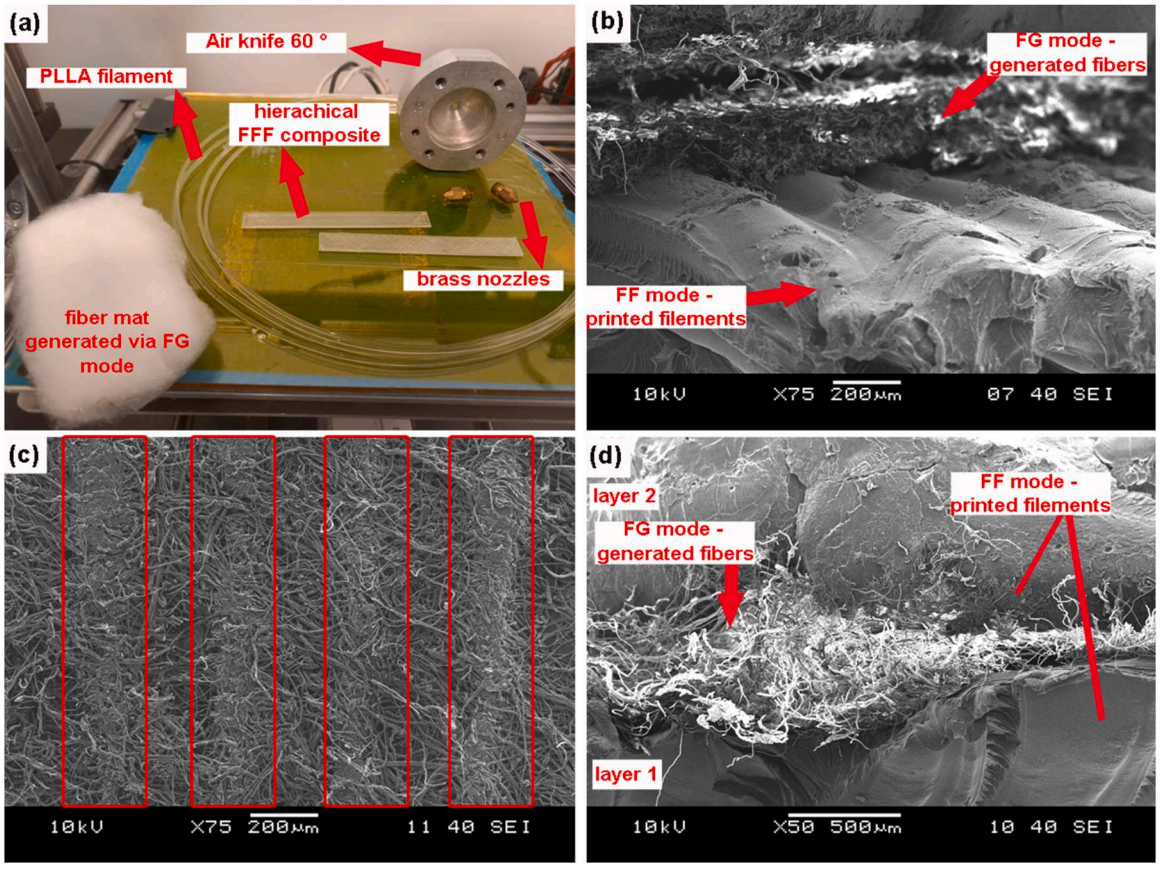

Fig. 15. Testing FF and FG modes; (a) optical image of the samples and used tools, (b) SEM images of FFF printed layer and fiber mat, (c) microstructure of a FFF printed hierarchical structure (red rectangles show FFF printed struts) and (d) cross-sections of the hierarchical microstructure consist of fibers and 3D printed struts.

Table 4
Comparison of the FFF 3D printed sample geometry with the CAD model.

	length [mm]	relative error [%]	thickness [mm]	relative error [%]	width [mm]	relative error [%]
1	79.73	0.34	1.49	0.67	9.96	0.40
2	79.37	0.79	1.52	1.33	9.97	0.30
3	79.42	0.73	1.55	3.33	10.06	0.60
4	79.35	0.82	1.54	2.67	10.01	0.10
5	79.57	0.54	1.54	2.67	10.09	0.90
CAD model	80.00		1.50		10.00	

and 3D print struts. The method makes it possible to continuously produce hierarchical FFF printed structures comprising nano-/submicron fibers and extruded filament using a single apparatus, as shown in Fig. 14 and Fig. 15 (Fig. S6). In this regard, we analyzed the geometry of the 3D printed sample and the CAD model (Fig. S9). Findings showed that the relative error between the 3D model and 3D printed samples is fairly small, as shown in Table 4. Findings implied that the developed apparatus could successfully generate objects based on a geometrical representation given by the CAD model.

Fig. 15(b-d) shows that the apparatus can successfully generate hierarchical structures consisting of fibers and 3D printed struts. In Fig. 15 (b), an SEM image shows fibers laid onto a 3D printed layer, while an SEM image of the 3D printed struts onto fiber mats is shown in Fig. 15 (c). The fibers and struts made of the same polymer (e.g., PLLA filament) had different melting characteristics observed in DSC tests. These findings prove that generated fibers and 3D printed struts had different microstructures, allowing them to adhere perfectly but not deteriorate during the FFF printing. Furthermore, fibers generated at FG mode stay intact with the 3D printed struts, and fibers fill the gap between adjacent struts, as shown in Fig. 15(d). This property would be an efficient solution for enhancing mechanical performance in the building direction (Fig. S6).

4. Conclusion

We introduced a novel 3D printing method that is capable of generating hierarchical structures of ultrafine fibers and solid layers of deposited material with a single printhead. It was shown that the printhead can be easily integrated into a commercial FFF printer without using expensive hardware and software. The device operates in two modes: filament fusion (FF) and fiber generation (FG) mode with simple switching between these. In the latter case, hot pressurized air blows and stretches the polymer melt into fine fibers. We proved that we could create hierarchical structures composed of solid (or even infill) parts and porous nano-/microfiber layers within a single 3D-printed object.

We can control the fiber mat structure in several ways. We simulated the airflow field by CFD and we proved that the air knife angle (35° vs. 60°) has a significant influence on the fiber strength. Decreasing the nozzle size and increasing the air pressure or air velocity decreases the fiber diameter considerably. Increasing hot air speed decreased the fiber diameter by up to 2-fold, while the fiber mat's specific strength was enhanced by up to 133%. With the aid of CFD simulations, we demonstrated that the air reaches supersonic velocities during the continuous FG mode. We showed that the fibers' glass transition temperature and crystallinity are 4 °C and 6% points higher than the feedstock filament. The ability to easily generate and combine porous ultrafine fibers and solid parts within a single 3D printed component makes it possible to fit in numerous applications, including but not limited to automotive, aerospace, defense, medical, pharmaceutical, textile and many more.

CRediT authorship contribution statement

Yahya Kara: Conceptualization, Methodology, Software, Data curation, Writing-Original draft preparation, Writing-Review & Editing, Visualization, Investigation, Formal analysis. **Norbert Krisztián Kovács:** Resources, Funding acquisition, Writing-Review & Editing. **Péter Nagy György:** Software, Writing-Reviewing and Editing, Validation. **Boros Robert:** Validation, Writing-Review & Editing. **Kolos Molnár:** Validation, Writing-Reviewing and Editing.

Declaration of Competing Interest

The authors declare that they have no known competing financial interests or personal relationships that could have appeared to influence the work reported in this paper.

Data availability

Data will be made available on request.

Acknowledgments

The authors thank Total Corbion PLA bv and Dr. G. Gobius du Sart, for supplying the PLA resins used in this work. The research reported in this paper is part of project no. BME-NVA-02, implemented with the support provided by the Ministry of Innovation and Technology of Hungary from the National Research, Development and Innovation Fund, financed under the TKP2021 funding scheme. The research reported in this paper was supported by the National Research, Development and Innovation Office (FK 138501, FK 134336 and K 138472). This paper was also supported by the János Bolyai Research Scholarship of the Hungarian Academy of Sciences (MTA).

Appendix A. Supporting information

Supplementary data associated with this article can be found in the online version at doi:10.1016/j.addma.2022.103315.

References

[1] H. He, K. Molnár, Fabrication of 3D printed nanocomposites with electrospun nanofiber interleaves, Addit. Manuf. 46 (2021), 102030, https://doi.org/10.1016/j.addma.2021.102030.
[2] T.W. Terry, C. Ian, D. Olaf, H. Ray, K. Joseph, M. Noah, Wohlers Report 2021: 3D Printing and Additive Manufacturing Global State of the Industry, (2021).
[3] T.W. Terry, C. Ian, D. Olaf, H. Ray, K. Joseph, M. Noah, Wohlers report 2022: 3D printing and additive manufacturing global state of the industry, (2022).
[4] V. Mohanavel, K.S. Ashraff Ali, K. Ranganathan, J. Allen Jeffrey, M.M. Ravikumar, S. Rajkumar, The roles and applications of additive manufacturing in the aerospace and automobile sector, Mater. Today.: Proc. 47 (2021) 405–409, https://doi.org/10.1016/j.matpr.2021.04.596.
[5] A.N. Solodov, J. Shayimova, D. Balkaev, A.S. Nizamutdinov, K. Zimin, A. G. Kiiamov, R.R. Amirov, A.M. Dimiev, High-throughput, low-cost and "green" production method for highly stable polypropylene/perovskite composites, applicable in 3D printing, Addit. Manuf. 59 (2022), 103094, https://doi.org/10.1016/j.addma.2022.103094.
[6] M. Javaid, A. Haleem, R.P. Singh, R. Suman, S. Rab, Role of additive manufacturing applications towards environmental sustainability, Adv. Ind. Eng. Polym. Res. 4 (4) (2021) 312–322, https://doi.org/10.1016/j.aiepr.2021.07.005.
[7] T.Q. Tran, F.L. Ng, J.T.Y. Kai, S. Feih, M.L.S. Nai, Tensile strength enhancement of fused filament fabrication printed parts: a review of process improvement approaches and respective impact, Addit. Manuf. 54 (2022), 102724, https://doi.org/10.1016/j.addma.2022.102724.
[8] ISO/ASTM 52900:2015 Additive manufacturing — General principles — Terminology.
[9] S.S. Crump, Apparatus and method for creating three-dimensional objects, Patent, US5121329A, USA, (1989).
[10] S. Yuan, S. Li, J. Zhu, Y. Tang, Additive manufacturing of polymeric composites from material processing to structural design, Compos. Part B: Eng. 219 (2021), 108903, https://doi.org/10.1016/j.compositesb.2021.108903.
[11] A. Cano-Vicent, M.M. Tambuwala, S.S. Hassan, D. Barh, A.A.A. Aljabali, M. Birkett, A. Arjunan, Á. Serrano-Aroca, Fused deposition modelling: Current status, methodology, applications and future prospects, Addit. Manuf. 47 (2021), 102378, https://doi.org/10.1016/j.addma.2021.102378.
[12] W. Johnston, B. Sharma, Additive manufacturing of fibrous sound absorbers, Addit. Manuf. 41 (2021), 101984, https://doi.org/10.1016/j.addma.2021.101984.

[13] Kamyab, G. Ghasemi, Fereidoon Khonakdar, Investigation into the shape memory behavior of peanut-pattern auxetic structures, Express Polym. Lett. 16 (2022) 679–693, https://doi.org/10.3144/expresspolymlett.2022.50.
[14] T. Spahiu, E. Canaj, E. Shehi, 3D printing for clothing production, 1558925020948216, J. Eng. Fibers Fabr. 15 (2020), https://doi.org/10.1177/1558925020948216.
[15] K. Chatterjee, T.K. Ghosh, 3D printing of textiles: potential roadmap to printing with fibers, Adv. Mater. 32 (4) (2020) 1902086, https://doi.org/10.1002/adma.201902086.
[16] Z. Zhang, H. He, W. Fu, D. Ji, S. Ramakrishna, Electro-hydrodynamic direct-writing technology toward patterned ultra-thin fibers: advances, materials and applications, Nano Today 35 (2020), 100942, https://doi.org/10.1016/j.nantod.2020.100942.
[17] F. Zhang, K. Cao, A. Zaeri, R. Zgeib, R.C. Chang, Design, fabrication, and analysis of spatially heterogeneous scaffold by melt electrospinning writing of poly (ε-Caprolactone), J. Appl. Polym. Sci. 139 (22) (2022) 52235, https://doi.org/10.1002/app.52235.
[18] Y. Kara, H. He, K. Molnár, Shear-aided high-throughput electrospinning: A needleless method with enhanced jet formation, J. Appl. Polym. Sci. 137 (37) (2020) 49104, https://doi.org/10.1002/app.49104.
[19] Botta Lopresti, C. La, Attinasi Settanni, Garofalo Gaglio, Physical and antibacterial properties of PLA electrospun mats loaded with carvacrol and nisin, Express Polym. Lett. 16 (2022) 1083–1098, https://doi.org/10.3144/expresspolymlett.2022.79.
[20] F. Zhang, K. Cao, A. Zaeri, R. Zgeib, R.C. Chang, Effects of scaffold design parameters on the printing accuracy for melt electrowriting, J. Manuf. Process. 81 (2022) 177–190, https://doi.org/10.1016/j.jmapro.2022.06.070.
[21] R. Farer, A.M. Seyam, T.K. Ghosh, S.K. Batra, E. Grant, G. Lee, Forming shaped/molded structures by integrating meltblowing and robotic technologies, Text. Res. J. 73 (1) (2003) 15–21, https://doi.org/10.1177/004051750307300103.
[22] R. Farer, A.M. Seyam, T.K. Ghosh, E. Grant, S.K. Batra, Meltblown Structures Formed by a Robotic and Meltblowing Integrated System: Impact of Process Parameters on Fiber Orientation and Diameter Distribution, Text. Res. J. 72 (12) (2002) 1033–1040, https://doi.org/10.1177/004051750207201201.
[23] Y. Kara, K. Molnár, A review of processing strategies to generate melt-blown nano/microfiber mats for high-efficiency filtration applications, J. Ind. Text. 51 (1_suppl) (2022) 137S–180S, https://doi.org/10.1177/15280837211019488.
[24] Y. Kara, K. Molnár, Revealing of process–structure–property relationships of fine polypropylene fiber mats generated via melt blowing, Polym. Adv. Technol. 32 (6) (2021) 2416–2432, https://doi.org/10.1002/pat.5270.
[25] Y. Kara, K. Molnár, Development of single-polypropylene composites interleaved with MWCNT-doped melt-blown fine fiber mats, Polym. Compos. 43 (8) (2022) 5208–5221, https://doi.org/10.1002/pc.26812.
[26] TamiCare, Speedy Additive Manufacturing of Fabrics, 2021. ⟨https://www.tamicare.com/manufacture⟩. (Accessed July 2022).
[27] Electroloom, The World's First 3D Fabric Printer, 2016. ⟨https://www.kickstarter.com/projects/electroloom/electroloom-the-worlds-first-3d-fabric-printer⟩. (Accessed July 2022).
[28] P. Romero-Araya, V. Pino, A. Nenen, V. Cárdenas, F. Pavicic, P. Ehrenfeld, G. Serandour, J.G. Lisoni, I. Moreno-Villoslada, M.E. Flores, Combining materials obtained by 3d-printing and electrospinning from commercial polylactide filament to produce biocompatible composites, Polymers 13 (21) (2021) 3806, https://doi.org/10.3390/polym13213806.
[29] H. He, M. Gao, B. Illés, K. Molnar, 3D printed and electrospun, transparent, hierarchical polylactic acid mask nanoporous filter, Int. J. Bioprinting 6 (4) (2020), https://doi.org/10.18063/ijb.v6i4.278.
[30] T. Kozior, A. Mamun, M. Trabelsi, L. Sabantina, Comparative analysis of polymer composites produced by FFF and PJM 3D printing and electrospinning technologies for possible filter applications, Coatings 12 (1) (2022) 48.
[31] Y. Yoon, C.H. Kim, J.E. Lee, J. Yoon, N.K. Lee, T.H. Kim, S.-H. Park, 3D bioprinted complex constructs reinforced by hybrid multilayers of electrospun nanofiber sheets, Biofabrication 11 (2) (2019), 025015, https://doi.org/10.1088/1758-5090/ab08c2.
[32] Y. Yu, S. Hua, M. Yang, Z. Fu, S. Teng, K. Niu, Q. Zhao, C. Yi, Fabrication and characterization of electrospinning/3D printing bone tissue engineering scaffold, RSC Adv. 6 (112) (2016) 110557–110565, https://doi.org/10.1039/C6RA17718B.
[33] T. Xu, K.W. Binder, M.Z. Albanna, D. Dice, W. Zhao, J.J. Yoo, A. Atala, Hybrid printing of mechanically and biologically improved constructs for cartilage tissue engineering applications, Biofabrication 5 (1) (2012), 015001.
[34] J.A. Smith, E. Mele, Electrospinning and additive manufacturing: adding three-dimensionality to electrospun scaffolds for tissue engineering, 674738-674738, Front Bioeng. Biotechnol. 9 (2021), https://doi.org/10.3389/fbioe.2021.674738.
[35] K.F. Eichholz, I. Gonçalves, X. Barceló, A.S. Federici, D.A. Hoey, D.J. Kelly, How to design, develop and build a fully-integrated melt electrowriting 3D printer, Addit. Manuf. 58 (2022), 102998, https://doi.org/10.1016/j.addma.2022.102998.
[36] D.B. Sitotaw, D. Ahrendt, Y. Kyosev, A.K. Kabish, Additive manufacturing and textiles—state-of-the-art, Appl. Sci. 10 (15) (2020) 5033, https://doi.org/10.3390/app10155033.
[37] H.C. Koch, D. Schmelzeisen, T. Gries, 4D textiles made by additive manufacturing on pre-stressed textiles—An overview, Actuators 10 (2) (2021) 31, https://doi.org/10.3390/act10020031.
[38] Y. Kara, N. Krisztián Kovács, K. Molnár, (In Hungarian) An apparatus for a fiber-forming 3D printer, a 3D printer incorporating such an apparatus, and a method of making a 3D printed polymer composite Patent, P2200146, Hungary, (2022).
[39] H.M. Krutka, R.L. Shambaugh, D.V. Papavassiliou, Analysis of a melt-blowing die: comparison of CFD and experiments, Ind. Eng. Chem. Res. 41 (20) (2002) 5125–5138, https://doi.org/10.1021/ie020366f.
[40] X. Hao, Y. Zeng, A review on the studies of air flow field and fiber formation process during melt blowing, Ind. Eng. Chem. Res. 58 (27) (2019) 11624–11637, https://doi.org/10.1021/acs.iecr.9b01694.
[41] S.V. Murphy, A. Atala, 3D bioprinting of tissues and organs, Nat. Biotechnol. 32 (8) (2014) 773–785, https://doi.org/10.1038/nbt.2958.
[42] H.-W. Kang, S.J. Lee, I.K. Ko, C. Kengla, J.J. Yoo, A. Atala, A 3D bioprinting system to produce human-scale tissue constructs with structural integrity, Nat. Biotechnol. 34 (3) (2016) 312–319, https://doi.org/10.1038/nbt.3413.
[43] A. Szabó, P.T. Nagy, G. Paál, Numerical simulation of an acoustically excited plane jet in an incompressible framework and comparison with experimental data, J. Acoust. Soc. Am. 147 (5) (2020) 3429–3443, https://doi.org/10.1121/10.0001256.
[44] P.T. Nagy, A. Szabó, G. Paál, A feedback model of the edge tone, using the adjoint Orr–Sommerfeld equation, J. Fluid Mech. 915 (2021) A13, https://doi.org/10.1017/jfm.2021.47.
[45] P. Tamás Nagy, G. Paál, On the sensitivity of planar jets, Int. J. Heat. Fluid Flow. 62 (2016) 114–123, https://doi.org/10.1016/j.ijheatfluidflow.2016.09.017.
[46] K.G. Schuchard, A. Pawar, B. Anderson, B. Pourdeyhimi, R.A. Shirwaiker, Multiphase CFD modeling and experimental validation of polymer and attenuating air jet interactions in nonwoven annular melt blowing, Ind. Eng. Chem. Res. (2022), https://doi.org/10.1021/acs.iecr.2c01710.
[47] Y. Yang, Y. Zeng, Measurement and comparison of melt-blowing airflow fields: nozzle modifications to reduce turbulence and fibre whipping, Polymers 13 (5) (2021) 719, https://doi.org/10.3390/polym13050719.
[48] S. Xie, W. Han, G. Jiang, C. Chen, Turbulent air flow field in slot-die melt blowing for manufacturing microfibrous nonwoven materials, J. Mater. Sci. 53 (9) (2018) 6991–7003, https://doi.org/10.1007/s10853-018-2008-y.
[49] J. Schmidt, S. Shenvi Usgaonkar, S. Kumar, K. Lozano, C.J. Ellison, Advances in melt blowing process simulations, Ind. Eng. Chem. Res. 61 (1) (2021) 65–85.
[50] D. Guo, H. Fan, Z. Zhu, K. Xiao, Numerical investigation into the effect of geometric shape of slot on air flow field in melt-blown for polymer fiber, J. Text. Inst. 113 (6) (2022) 1133–1141, https://doi.org/10.1080/00405000.2021.1916222.
[51] T. Tábi, S. Hajba, Cross effect of natural rubber and annealing on the properties of poly (Lactic Acid), Period. Polytech. -Mech. Eng. 64 (4) (2019) 270–277, https://doi.org/10.3311/PPme.12825.
[52] ASTM E1356–08(2014):Standard Test Method for Assignment of the Glass Transition Temperatures by Differential Scanning Calorimetry.
[53] T. Kim, S. Lee, G.B. Kim, D. Hong, J. Kwon, J.-W. Park, N. Kim, Accuracy of a simplified 3D-printed implant surgical guide, e2. J. Prosthet. Dent. 124 (2) (2020) 195–201, https://doi.org/10.1016/j.prosdent.2019.06.006.
[54] M.M. Hanon, L. Zsidai, Q. Ma, Accuracy investigation of 3D printed PLA with various process parameters and different colors, Mater. Today.: Proc. 42 (2021) 3089–3096, https://doi.org/10.1016/j.matpr.2020.12.1246.
[55] Y. Yang, H. Huang, Y. Zeng, Turbulence of melt-blowing airflow field: comparison of a convergent jet and a typical free jet, Phys. Fluids 33 (7) (2021), 075107, https://doi.org/10.1063/5.0055571.
[56] H.M. Krutka, R.L. Shambaugh, D.V. Papavassiliou, Effects of die geometry on the flow field of the melt-blowing process, Ind. Eng. Chem. Res. 42 (22) (2003) 5541–5553, https://doi.org/10.1021/ie030457s.
[57] M. Du, K. Jariyavidyanont, R. Zhang, A.M. Rhoades, C. Schick, R. Androsch, Thermal stability of shear-induced crystal nuclei of Poly(l-lactic acid, ACS Appl. Polym. Mater. 4 (10) (2022) 7823–7833, https://doi.org/10.1021/acsapm.2c01365.
[58] A. Jalali, M.A. Huneault, M. Nofar, P.C. Lee, C.B. Park, Effect of branching on flow-induced crystallization of poly (lactic acid, Eur. Polym. J. 119 (2019) 410–420, https://doi.org/10.1016/j.eurpolymj.2019.07.045.